Journal of Materials Chemistry A

Layered Graphene/Mesoporous Carbon Heterostructures with Improved Mesopore Accessibility for High Performance Capacitive Deionization

Journal:	*Journal of Materials Chemistry A*
Manuscript ID	TA-ART-04-2018-003114.R1
Article Type:	Paper
Date Submitted by the Author:	21-Jun-2018
Complete List of Authors:	Noonan, Owen; The University of Queensland, Liu, Yang; Australian Institute for Bioengineering and Nanotechnology (AIBN), University of Queensland Huang, Xiaodan; The University of Queensland, Australian Institute for Bioengineering and Nanotechnology Yu, Chengzhong; University of Queensland, Australian Institute for Bioengineering and Nanotechnology (AIBN)

SCHOLARONE™
Manuscripts

Journal of Materials Chemistry A

ARTICLE

Layered Graphene/Mesoporous Carbon Heterostructures with Improved Mesopore Accessibility for High Performance Capacitive Deionization

Received 00th January 20xx,
Accepted 00th January 20xx

DOI: 10.1039/x0xx00000x

www.rsc.org/

Owen Noonan, Yang Liu, Xiaodan Huang,* and Chengzhong Yu*

Rational design of porous carbon electrodes remains central to the development of high performance capacitive deionization (CDI) technology. Efficient electrosorption in CDI relies on the unimpeded transfer of salt ions from the bulk water to carbon pore surfaces. Improving mesopore accessibility by shortening pore lengths and opening pore apertures is expected to facilitate the ion diffusion and promote the CDI performance, however a material platform offering controls of these parameters has not been applied to CDI systems. Herein, layered heterostructures consisting of graphene sheets and conformal mesoporous carbon layers are prepared via an interfacial Stöber templating process followed by post-activation. The mesopore opening and mesopore length are simultaneously controlled to study their influences on CDI properties. It is demonstrated that the open mesopore and short mesopore length are determinant factors for high ion diffusivity and high salt adsorption capacity (SAC, 24.3 mg g^{-1}), which illuminates new avenues to develop high performance CDI electrode materials.

Introduction

Capacitive deionization (CDI) is an emerging technology for the efficient desalination of brackish and saline water.[1-3] In contrast to traditional membrane-based and thermal processes, CDI does not rely on high pressures or temperatures, but rather separates salt ions directly from feed water under ambient conditions through reversible, low-voltage electrosorption on porous carbon electrodes.[4] While the gains in energy efficiency, reduced operating costs and bi-directional scalability are quite appealing, further improvement in desalination performance relies primarily on the development of advanced materials which meet the specific needs of CDI processes.[5-6]

The mechanism of salt removal in conventional CDI centres on the electrosorption of ions at electric double layers (EDL), which is comparable to the charge storage mechanism in electric double layer capacitors (EDLCs).[3] As a result, material properties which favour high capacitance in EDLCs, such as large surface area, high electronic conductivity, and good wettability, also contribute to high salt adsorption capacity (SAC) in CDI. Mesoporous nanostructured carbons which exhibit such properties have recently been extensively applied in CDI, including ordered mesoporous carbons,[7-9] three-dimensional graphenes,[10-13] porous carbon spheres,[14] hollow mesoporous carbon spheres,[15-16] hierarchically porous carbon monoliths[17-18] and activated carbon fibres.[19-22]

The major distinction between CDI and EDLC electrosorption processes however, is the vastly increased ion diffusion length required for the transportation of ions from the bulk feed solution into the pores of CDI electrodes, as compared with the typically much shorter diffusion distance in EDLCs.[23] This is because the typical ionic concentrations of brackish feed water for CDI (2 to 10 mM) can be approximately three orders of magnitude lower than typical EDLC electrolytes (2 to 10 M). As illustrated in Figure 1 a and b, the low concentration CDI solution results in a potentially large influx of ions (~20 to 200 times that of the "in-pore" ions before charge) into mesoporous electrodes, while the high concentration EDLC electrolytes induce only short-range ion rearrangement in the vicinity of the mesopore surface. This means, for CDI, the attainment of equilibrium adsorption at the EDL is largely dependent on the long range ionic transportation across the solution-electrode interface.

With this in mind, the mesopore accessibility as determined by pore size, pore aperture and pore length become a critical consideration for performance improvements in CDI material design. However, to date, a material platform which provides for evaluation of the mesopore opening and mesopore length has not been applied to CDI systems. Conventional porous carbon materials, such as ordered mesoporous carbons[7-9,24,25] and their composites,[26] suffer from relatively long mesopore

[a] Australian Institute for Bioengineering and Nanotechnology, The University of Queensland, Brisbane QLD 4072, Australia
*Corresponding author: x.huang@uq.edu.au (Xiaodan Huang); c.yu@uq.edu.au (Chengzhong Yu)

† Footnotes relating to the title and/or authors should appear here.
Electronic Supplementary Information (ESI) available: [details of any supplementary information available should be included here]. See DOI: 10.1039/x0xx00000x

This journal is © The Royal Society of Chemistry 20xx

Please do not adjust margins

channels (hundreds of nanometers to microns) that are unfavourable for high level ionic influx and thus result in impeded CDI performance (~15 mg g^{-1} at 500 mg L^{-1} NaCl). Hierarchical pore structuring has been investigated as a method to increase ionic accessibility of the CDI electrodes. Hierarchical porous carbons have been prepared by compositing of mesoporous carbon with graphene.[18] However, the carbon layer thickness and mesopore opening are not controlled, which leads to restricted ionic diffusion pathways and a low capacity of 6.18 mg g^{-1} at 25 mg L^{-1} NaCl. Layered porous carbon nanostructures with thin thickness present a promising approach to improve the pore accessibility in CDI electrodes. However, current research on such structured CDI materials is primarily focused on the improvement of surface area .[27]

In this work, we report the preparation of layered graphene/mesoporous carbon (G@MC) heterostructures for high performance CDI applications. These materials are synthesized through a simple interfacial Stöber co-deposition method, followed by post-activation. The mesopore opening and mesopore length have been systematically controlled and the influences of these structural features on CDI performances are investigated. The open mesopore structure and short mesopore length are identified as critical factors determining the high mesopore accessibility and ion diffusivity (Figure 1c). The material featuring the large open mesopore (5-7 nm) and short pore length (29.0 ± 1.3 nm) demonstrates an outstanding SAC of 24.3 mg g^{-1} at 1.5 V in 500 mg L^{-1} NaCl, superior to other porous carbon materials used in CDI systems.[7-26]

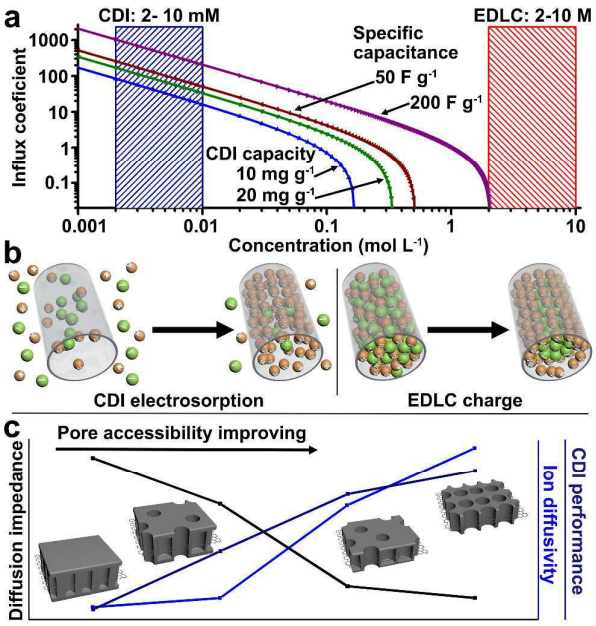

Figure 1. (a) The correlation between ion influx and electrolyte concentration in both CDI and EDLCs (see the discussion in supplementary information). (b) The illustration of the electrosorption and charge processes in CDI and EDLCs, respectively. (c) The schematic demonstration of the pore accessibility control and its influences on ion diffusion and CDI performance.

Experimental section

Material Synthesis

G@MC heterostructures were prepared through an interfacial modified in-situ Stöber templating method followed by post-activation (Figure S1). In a typical procedure, graphene sheets synthesized by the electrochemical exfoliation method[28] (150 mg or 200 mg) were dispersed in a solution containing ethanol (AR grade), H_2O (18.2 MΩ.cm) and NH_4OH (Vetec, 25% w/w) (80mL, 7:1:0.3 v/v) under constant stirring. Dopamine hydrochloride (Sigma, 400mg) was added immediately preceding the dropwise addition of TEOS (Aldrich, 98%, 2 mL) and the mixture was stirred at room temperature for 12 hours. The resulting precipitate was rinsed three times in water and once in ethanol by centrifugation/redispersion cycles before drying overnight in a 50 °C oven. The dried precipitate was heated to 800 °C for 5 hours (ramp rate 2 °C/min) under nitrogen flow. G@MC composites were obtained after removal of silica *via* etching in 1 M NaOH solution at 70 °C for 24 hours. In the case of G@MC-O-thin, further activation was carried out by a secondary thermal treatment of G@MC at 800 °C for 3 h under hydrated nitrogen flow to enlarge pore openings.

Structure Characterization

The morphology and structure of G@MC samples were investigated by field emission scanning electron microscope (FESEM, JEOL 7800) operated at 1kV and transmission electron microscope (TEM, Hitachi HT7700) at 120 kV. Energy Dispersive Spectroscopy (EDS) mapping was obtained *via* scanning transmission electron microscopy (STEM). Nitrogen adsorption isotherms were measured at 77 K using a TriStar II Surface Area and Porosity analyser (Micromeritics). G@MC samples were degassed under vacuum for 12 h at 180 °C before analysis. The specific surface areas were obtained by the Brunauer-Emmett-Teller (BET) method using adsorption data at a relative pressure range between 0.05 and 0.25. Pore size distributions were determined using the Barrett-Joyner-Halenda (BJH) method. The pore volumes were calculated by the amount of nitrogen adsorbed at the highest relative pressure (~0.99). X-ray photoelectron spectra (XPS) were collected on a Kratos Axis ULTRA X-ray photoelectron spectrometer (Perkin-Elmer).

Electrochemical Characterization

Working electrodes consisted of G@MC materials, acetylene black, and polytetrafluoroethylene (PTFE) mixed in an 80:10:10 weight ratio and pressed onto graphite foil current collectors. The weight of active material per electrode was approximately 1 mg occupying an area of 1 cm^2. Electrochemical measurements including cyclic voltammetry (CV) and galvanostatic charge/discharge (GC) and Electrochemical

This journal is © The Royal Society of Chemistry 20xx

Please do not adjust margins

impedance spectroscopy (EIS) tests were performed on a Solartron Multistat electrochemical workstation using a 3-electrode cell setup in 0.5 M NaCl electrolyte with platinum wire and Ag/AgCl (0.5 M KCl) electrodes as counter and reference electrodes, respectively. The frequency range analysed was 0.1 – 100000 Hz with amplitude ± 5 mV. Diffusion coefficients were calculated according to equation 1:

$$D = \frac{R^2\,T^2}{2A^2n^4F^4c^2\sigma^2} \quad (1)$$

Where R is the gas constant, T is temperature (K), A is the electrode area (cm^2), n is the number of charges per ion (n=1), F is the Faraday constant, c is the ionic concentration in the electrode (mol L^{-1}) and σ is the Warburg coefficient.

CDI Performance Measurement

A lab made flow-by CDI apparatus was constructed for deionization testing. Apparatus details can be found in the supplementary information (Figure S2 a). Identical CDI electrodes were fabricated by mixing G@MC materials, acetylene black and PTFE in an 80:10:10 weight ratio. The mixture containing 50 mg active material was cast onto graphite foil current collectors to cover an area of 50 mm x 100 mm. Saline water (25 mL) was continuously recirculated through the CDI cell using a peristaltic pump at a flow rate of 25 mL min^{-1}. Ionic conductivity measurements were obtained using a Horriba Laqua F-70 conductivity meter (Figure S2 b). A Solartron Multistat electrochemical workstation was used to the control voltage and record current flow supplied to the cell.

SAC is calculated according to equation 2:

$$SAC = \frac{(C_u - C_v)V}{m} \quad (2)$$

Where C_u is the initial concentration (mg L^{-1}), C_v is the final concentration at time t (mg L^{-1}), V is the volume of NaCl solution (L) and m is the active mass of the electrodes (g).

Charge efficiency (Λ) is calculated according to equation 3:

$$\Lambda = \frac{\Gamma \times F}{\Sigma} \quad (3)$$

Where Γ is the molar salt adsorption capacity (mol g^{-1}), F is faradays constant (96 485 C mol^{-1}), Σ is the total charge transferred between the electrodes (C g^{-1})

Results and discussion

G@MC heterostructured materials with tuneable pore structures and mesoporous carbon layer thicknesses were prepared by independently varying the amount of tetraethyl orthosilicate (TEOS) and graphene in a one-pot Stöber templating synthesis containing polydopamine (PDA) precursors (details in experimental section, Figure S1 and Table S2). By increasing the TEOS amount from 1 to 2 mL while keeping the graphene amount constant, a relatively thick porous carbon layer is formed, featuring mesopore structures which can be tuned from closed (G@MC-C-thick) to partially open (G@MC-PO-thick) at the surface. By increasing the graphene amount from 150 mg to 200 mg, a relatively thin carbon layer is formed with partially open mesopores (G@MC-PO-thin). Post synthesis thermal activation of G@MC-PO-thin increases the density and size of mesopore openings while leaving the thickness of the mesoporous carbon coating unchanged (G@MC-O-thin).

SEM images reveal all four G@MC materials exhibit the lamellar morphology with porous surface structures (Figure 2 a-d). G@MC-O-thin (Figure 2a) displays a thin mesoporous coating with sections of the underlying graphene scaffold exposed. A large number of mesopore openings can be clearly observed on the carbon surface with diameters measuring approximately 8-10 nm. In comparison, G@MC-PO-thin (Figure 2b) displays a more scattered population of open and semi-open mesopores embedded in a continuous carbon layer with pore openings decreased to 4-6 nm. G@MC-PO-thick (Figure 2c) also exhibits surface pores with semi-open structures, while in contrast, G@MC-C-thick (Figure 2d) displays a relatively smooth and unbroken surface without obvious mesopore openings. Some pore-like features can be observed in the SEM micrographs which result from the escape of backscattered electrons from pore structures below the thin carbon surface.

This journal is © The Royal Society of Chemistry 20xx

Please do not adjust margins

Journal of Materials Chemistry A

ARTICLE

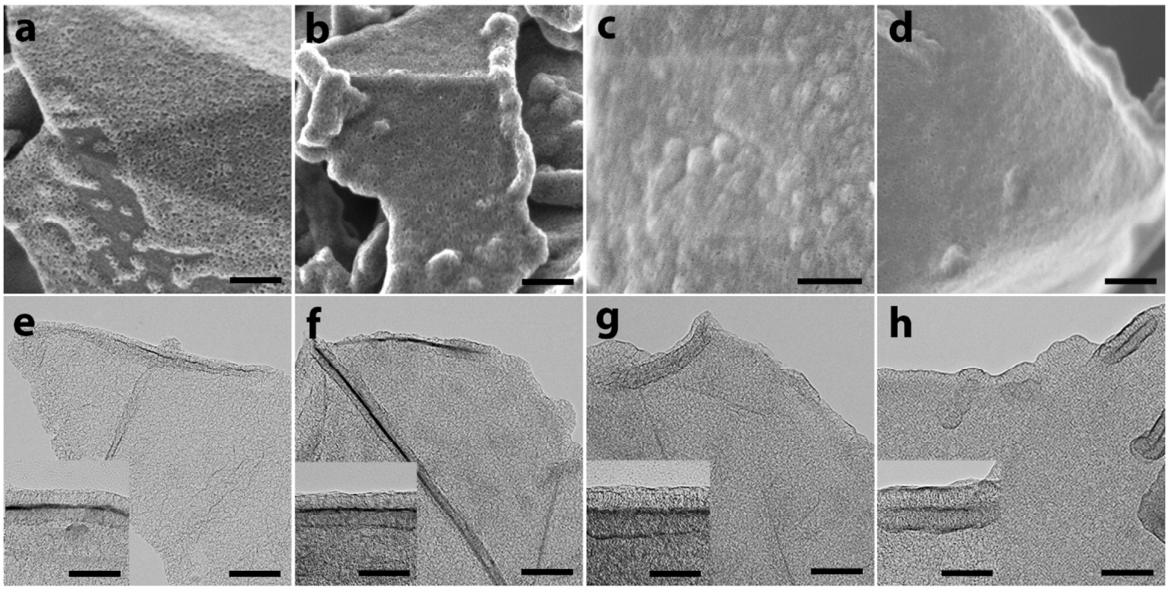

Figure 2. (a-d) SEM (top) and (e-h) TEM images (bottom) of G@MC-O-thin (a, e), G@MC-PO-thin (b, f), G@MC-PO-thick (c, g) and G@MC-C-thick (d, h). Insets in e-h show expanded view of edge regions. Main scale bars: 200 nm, inset scale bars: 100 nm.

TEM provides further structural information for the four G@MC materials. Figure 2e (G@MC-O-thin) shows large sheets covered in mesoporous structures, while higher magnification of an edge region (Figure 2e, inset) reveals a graphene layer coated by a mesoporous carbon layer with thickness measuring approximately 29.1 nm, consistent with the surface profile visible in SEM. G@MC-PO-thin (Figure 2f) exhibits similar lamellar structure with mesoporous carbon layer thickness of 29.7 nm (Figure 2f, inset). For G@MC-PO-thick (Figure 2g) and G@MC-C-thick (Figure 2h), large-area mesoporous sheets are also visible, while the high magnification of the edge regions (insets of Figure 2 g and h) reveal an increase in thickness of the carbon layer for both materials to approximately 42.3 nm and 40.1 nm, respectively, which is consistent with the increased mass ratio of mesoporous carbon precursors to graphene used in the synthesis. One important difference apparent in the G@MC-C-thick sample is the dense carbon coating enclosing the outer boundary of the mesoporous carbon layer (Figure 2h), a feature that is absent in the other three samples (Figure 2e, f and g). This dense surface layer measures approximately 5 nm in thickness and forms a continuous barrier over the mesoporous structure beneath. This observation is consistent with surface features characterized by SEM and can be attributed to the decrease of silica content that promotes the deposition of excess PDA at the surface of the G@PDA/SiO_2 composites.

X-ray photoelectron spectroscopy (XPS) confirms the presence of carbon (90.1 at. %), nitrogen (4.2 at. %) and oxygen (5.2 at. %) in the typical G@MC-O-thin sample (Figure S3 a, Table S1). High resolution scans of the N1s peak for a characteristic sample confirms the majority of nitrogen (> 50 at. %) is present as in-ring graphitic nitrogen (Figure S3 b), followed by pyridinic and pyrrolic structures which is consistent with previous findings on the pyrolysis of polydopamine.[29] The homogeneous spatial distribution of nitrogen and oxygen throughout the carbon matrix is confirmed by elemental mapping from EDS spectroscopy (Figure S4), further supporting the findings from XPS.

Nitrogen adsorption isotherms for all four G@MC materials display type IV profiles with hysteresis loops indicating mesoporosity in the carbon layers (Figure 3a). High surface areas of 1270 cm^2g^{-1}, 1100 cm^2g^{-1}, 924 cm^2g^{-1} and 807 cm^2g^{-1} are observed for G@MC-O-thin, G@MC-PO-thin, G@MC-PO-thick and G@MC-C-thick, respectively, which are substantially higher than those previously reported for G@MC materials applied in CDI (685.2 cm^2g^{-1}).[26] Pore size distributions calculated from the adsorption branch (Figure 3b, Table 1) are centred at 6.4 nm, 5.9 nm, 5.9 and 2.9 nm for the four samples, respectively. Interestingly, a distinct distribution of smaller pores centred at 2.9 nm can be detected for all four samples which may arise from primary silica particles in the synthesis, as previously observed in similar Stöber templating systems.[30, 31]

Please do not adjust margins

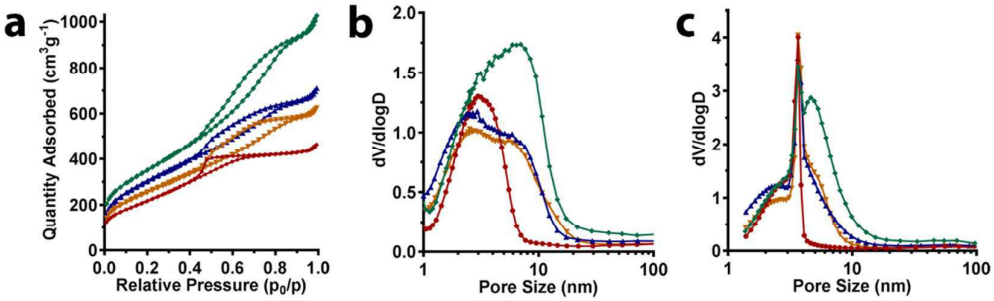

Figure 3. Nitrogen adsorption isotherms (a), pore size distributions derived from the adsorption (b) and desorption branches (c) for G@MC-O-thin (green ♦), G@MC-PO-thin (blue ▲), G@MC-PO-thick (orange ▼) and G@MC-C-thick (red ●).

In order to better elucidate the detailed mesopore structure, pore size distributions derived from the desorption branches were determined (Figure 3c, Table 1).These data are derived from the capillary evaporation of liquid nitrogen from flooded pores as partial pressure is decreased and thus provide a more accurate indicator of the size of mesopore openings as compared to adsorption branch pore size analysis.[32] A sharp pore distribution centred at 4.6 nm can be observed for the open mesopore sample (G@MC-O-thin), which supports the SEM observations of larger mesopore entrances in this sample. In contrast, G@MC-PO-thin and G@MC-PO-thick exhibit less well-defined distributions centred below 4 nm and are partly occluded by the false peak at 3.7 nm, indicating mesopore openings in these samples are smaller and less abundant than those of G@MC-O-thin. Finally, the desorption pore size distribution for G@MC-C-thick does not reveal any pore volume above 3.7 nm supporting SEM evidence that this sample does not contain significant number of open mesopores.

To investigate the structure of the mesoporous carbon layer in finer detail, the silica/polymer composites (G@MC precursors) were either calcined in air at 500 ^{o}C (Figure 4 a-d) or washed with 0.1 M NaOCl to selectively remove PDA while leaving silica intact.[33] (Figure 4 e-h). After these treatments, PDA has been removed leaving only graphene sheets and silica structures as witness to the templating process of G@MC materials. Calcination of G@MC-O-thin and G@MC-PO-thin precursor composites reveals plate-like structures composed of fused silica aggregates (Figure 4 a, b). Interestingly, when the samples are washed in NaOCl instead of calcined (Figure 4 e, f), a similar morphology to the calcined structure is obtained, however individual silica aggregates are more clearly visible. These particles measure 5-6 nm in diameter which suggests they may originate from the secondary clustering of primary silica particles during co-deposition of silica and PDA.[30, 31, 34] From magnification of the upturned edge regions (insets of Figure 4 a, b, e, f) rod-shaped arrangements of silica particles can be seen axially aligned to the graphene surface. The links formed between spikes allow the silica to remain in formation on the surface of graphene sheets. The retention of a cross linked plate-like morphology indicates that secondary particles have undergone fusion with neighbouring particles during the co-deposition stage rather than during calcination. The thickness of the silica region measures approximately 41 nm which exceeds the thickness of the corresponding templated carbon layer (~29 nm), confirming that silica templates protrude through the surface region of the composite materials. This suggests that silica spikes directly template mesopore openings in G@MC materials. Accurate measurement of carbon and silica thickness are presented in Table 1 and Figure S5.

Please do not adjust margins

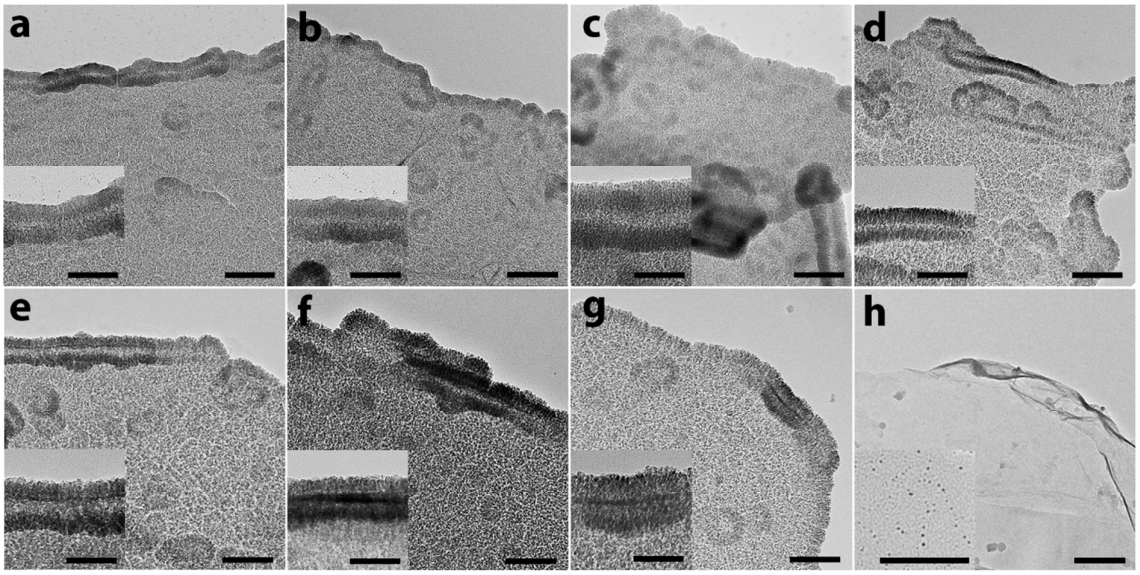

Figure 4. TEM images showing structures obtained after calcination at 500 °C (top) and PDA dissolution in 0.1 M NaOCl (bot-tom) of G@MC precursor composites. G@MC-O-thin (a,e) and G@MC-PO-thin (b,f) G@MC-PO-thick (c,g) and G@MC-C-thick (d,h). Insets show magnification of upturned sheet edge (a-f) and isolated silica primary particles (g-h). Main scale bars: 200 nm, inset scale bars: 100 nm.

The calcination products of G@MC-PO-thick precursors (Figure 4c) exhibit similar structures to those observed for the thin layer samples, with the exception of an increased silica layer thickness from approximately 41 nm to 51.3 nm (Figure 4c inset) which partially exceeds the thickness of the corresponding carbon layer (42.3 nm) indicating silica also templates mesopore openings in this material. In contrast, calcination products for the G@MC-C-thick precursor (Figure 4d and inset) again reveal sheet like structures covered with axial spikes but with lengths below the thickness of the corresponding carbon structures (33.6 and 40.1 nm, respectively). This is consistent with indications from SEM and nitrogen adsorption that silica templated mesoporosity does not extend through the surface of G@MC-C-thick. Notably, washing with NaOCl for this sample produces a smooth particle-free sheet of graphene (Figure 4h). Isolated primary particles measuring 2-3 nm can also be observed on the TEM carbon grid at higher magnifications (Figure 4h inset). This size corresponds closely with previous observations of primary silica particles in classical Stöber[31, 35] and mixed Stöber systems.[30] These observations indicate that small silica primary particles are responsible for the templating of pores in G@MC-C-thick. In this process they are individually isolated by the PDA matrix during the co-deposition process and are then free to disperse from the graphene sheet upon removal of PDA. On the other hand, when PDA is removed by calcination, silica primary particles undergo sintering and partial fusion allowing retention of their arrangement on the graphene (Figure 4d.). In the case of higher TEOS amounts however, primary particle concentration is sufficient for the formation of secondary silica clusters measuring 4-6 nm in diameter.[30] These particles can occasionally be observed in isolation alongside sheet-like structures after washing with NaOCl (Figure S6). The secondary particles co-deposit on the graphene surface in a semi-crosslinked network, from which only a small fraction may be released after removal of PDA. The observation of secondary clustering and fusion during co-deposition provides further justification for the increase in pore size in resulting mesoporous carbon structures and is supported by previous findings on pore size control via the co-deposition of silica with PDA.[30] Importantly, these results indicate the mesopore structures formed in the open and partially open G@MC materials are the result of aligned silica rods protruding above the carbon layer. This confirms the resulting mesopore structures are open and accessible.

The above investigations demonstrate that the mesoporous structure parameters of G@MC materials are primarily controlled by adjusting graphene and TEOS content in the synthesis. Increasing the graphene amount (from 150 to 200 mg) provides more surfaces for the deposition of carbon and silica precursors, resulting in the growth of a thinner mesoporous carbon layer. On the other hand, by adjusting the TEOS content (1 or 2 mL), the concentration of silica primary particles varies, leading to the formation of either isolated silica particles or secondary silica clusters as mesopore templates. The isolated silica particle templates are responsible for the closed mesopores, while the silica cluster templates create partially open mesopores. The additional activation step further opens the pore aperture to form open mesopores.

Table 1. Structural properties of four G@MC materials.

	Mesopore opening	$Carbon_{layer}$ nm	$Silica_{layer}$ nm	D_{des} nm	$D_{ads.}$ nm	S_{BET} $m^2 g^{-1}$	V_{pore} $cm^3 g^{-1}$
G@MC-O-thin	open	29.0 ± 1.3	40.9 ± 1.5	4.6*	2.9-6.4*	1270	1.60
G@MC-PO-thin	partially open	29.7 ± 1.0	41.4 ± 1.7	n/a	2.9*-5.9	1100	1.13
G@MC-PO-thick	partially open	42.3 ± 1.4	51.3 ± 1.6	n/a	2.9*-5.9	924	0.99
G@MC-C-thick	closed	40.1 ± 0.8	33.6 ± 1.4	n/a	2.9	807	0.75

*denotes dominant peak.

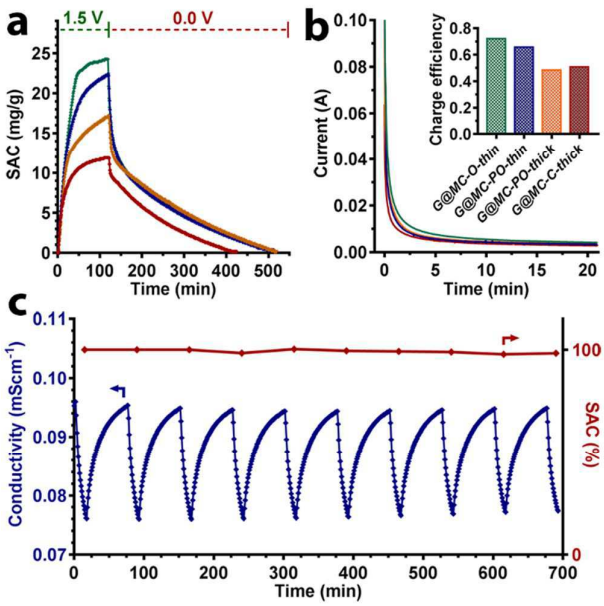

Figure 5. (a) CDI capacity for G@MC-O-thin (green ♦), G@MC-PO-thin (blue ▲), G@MC-PO-thick (orange ▼) and G@MC-C-thick (red ●). (b) initial current response profiles for G@MC-O-thin (green), G@MC-PO-thin (blue), G@MC-PO-thick (orange) and G@MC-C-thick (red). Inset in (b) shows corresponding charge efficiency. (c) Reversible electrosorption for G@MC-O-thin at 500 mg L^{-1} NaCl at 1.2 V - 0 V (left axis) and SAC retention (right axis) over 10 cycles.

CDI electrode performance of these materials is evaluated through comparison of SAC at a standard influent NaCl solution with the concentration of 500 mg L^{-1}. The time dependent decreases in concentration of the recirculating saline solutions are shown in Figure S9. G@MC-O-thin exhibits the highest SAC of 24.3 mg g^{-1} after 120 min electrosorption at 1.5V (Figure 5a). In contrast, G@MC-PO-thin reaches only 22.2 mg g^{-1} under the same condition, which can be attributed to the reduced mesopore opening feature and the slightly decreased surface area. Compared with G@MC-PO-thin, G@MC-PO-thick shows an even lower SAC of 17.1 mg g^{-1}, confirming that the increased mesoporous carbon layer thickness significantly reduces electrosorption efficiency. Furthermore, there is a notably sharp decrease in SAC observed for the G@MC-C-thick sample (11.8 mg g^{-1}), when compared to the partially open mesopore sample with the same layer thickness (G@MC-PO-thick), suggesting a largely suppressed electrosorption process in G@MC-C-thick material.

In order to extricate the influence of surface area from that of other material properties, SAC results were normalised by BET surface area for the different samples (Table 2, Figure S7). Both thin layer samples show a higher normalised SAC as compared with either of the thick layer samples, which provides convincing evidence that decreasing mesoporous carbon layer thickness enhances SAC. Moreover, comparison of the two thick layer samples reveals a significantly lower normalised SAC value for the closed mesopore sample (G@MC-C-thick), which indicates that, irrespective of thickness or surface area, increasing size and density of mesopore apertures is also critical for enhanced SAC.

Current response profiles for the four samples and corresponding charge efficiencies (inset) are shown in Figure 5b. G@MC-O-thin exhibits the highest charge efficiency of the four materials indicating the higher electrosorption charge utilisation and the reduction of parasitic side reactions on the electrode material itself. This may arise from the increased stabilisation of mesoporous carbon layer during activation. The increased charge efficiency of G@MC-PO-thin as compared to the thick layer materials provides indication that the decreased mesoporous carbon to graphene weight ratio reduces the opportunity for parasite side reactions in the carbon matrix. Another source of non-elctrosorpitive charge consumption in CDI results from co-ion expulsion from electrodes with the same polarity. The increase in charge efficiency observed for the thin layer materials may be attributed to the reduced ion diffusion lengths in this material which could plausibly lower ambient adsorption of co-ions. Figure 5c shows the electrosorption cycling profile for G@MC-O-thin, which demonstrates salt uptake is highly reversible and electrode materials achieve near 100% retention of capacity over ongoing cycling. These data confirm the suitability of G@MC-O-thin sample as functional high performance CDI electrode material.

To understand the reason for the SAC difference of G@MC materials, their electrochemical behaviours were investigated by cyclic voltammetry (CV) and electrochemical impedance spectroscopy (EIS) analyses. CV curves for G@MC-O-thin exhibit well defined symmetrical rectangular profiles at increasing scan rates from 10-150 mVs^{-1} (Figure 6a), indicating that charge immobilisation on the electrodes is reversible and predominantly capacitive rather than faradaic. Comparison of the CV curves for the four materials at 100 mVs^{-1} shows an increase in area from G@MC-C-thick to G@MC-O-thin reflecting the increase in specific capacitance for the open pore thin layer sample (Figure 6b). Galvanic cycling at 10 A g^{-1} reveals well defined triangular charge-discharge profiles confirming the good capacitive behaviour of the electrodes (Figure 6c). The lack of substantial IR drop indicates electrodes are not overly affected by polarisation during charging even at

Please do not adjust margins

relatively high current densities. Specific capacitances measured at varying current densities were normalised by surface area, in order to more clearly evaluate the role of other textural properties independent of surface area. (Figure 6e, Table 2). In general, normalised capacitance is found to increase consistently from G@MC-C-thick though to G@MC-O-thin in accordance with increased mesopore accessibility. The highest normalised capacitance was recorded for G@MC-O-thin, and when compared to that of G@MC-PO-thin indicates that the opening of mesopores due to activation has contributed significantly to the enhanced capacitive performance.

Electrochemical impedance spectroscopy (EIS) provides more detailed information on the behaviour of electrosorption processes in G@MC composites. In the high frequency region of the Nyquist plot (Figure 6d) the diameter of the semicircle is correlated to the charge transfer resistance (R_{ct}).[36] Comparison of R_{ct} values for the four materials (Figure 6f, Table 2) reveals a decrease in R_{ct} in concert with the decreased restriction of pore accessibilities. This result confirms the importance of open meso-porosity and short mesopore channel in reducing charge transfer resistance. The linear low frequency region of the Nyquist plot provides information on the diffusion resistance encountered by ions migrating through the electrode, also known as the Warburg impedance.[37] By plotting measured resistance values against the inverse square root of frequency (Figure S8), the Warburg co-efficient (σ) can be obtained, thus allowing calculation of ion diffusion coefficients (D) according to equation 1 (Figure 6f).[38, 39] Diffusion coefficients are found to be highest for G@MC-O-thin with a value of 4.37 x 10^{-14} cm^2 s^{-1} and decrease to 0.36 x 10^{-14} cm^2 s^{-1} for G@MC-C-thick, indicating the reduced ion diffusivity and mesopore accessibility. Therefore, the ion influx in G@MC-O-thin electrode would be much more convenient over other G@MC materials, leading to its high CDI capacity. This observation validates the critical role of open mesopore structure and short mesopore length for the improved pore accessibility, high ion diffusivity and consequently superior CDI performance (Figure 1c).

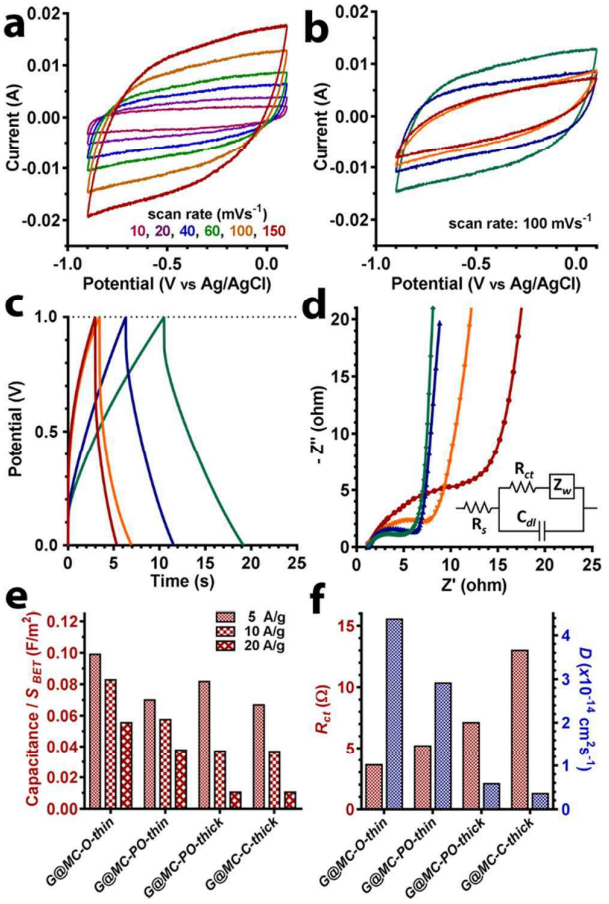

Figure 6. (a) Cyclic voltammetry scans at varying scan rates for G@MC-O-thin. (b) 100 mVs^{-1} Cyclic voltammetry scans, (c) Galvanic charging cycles at 10 A g^{-1} and (d) Nyquist plots for for G@MC-O-thin (green ♦), G@MC-PO-thin (blue ▲), G@MC-PO-thick (orange ▼) and G@MC-C-thick (red ●). The EIS frequency range was 0.1 – 100000 Hz with amplitude ± 5 mV. Inset in (d) shows equivalent circuit diagram, where R_s is the series resistance, R_{ct} is the charge transfer resistance, Z_w is the Warburg impedance and C_{dl} is the double layer capacitance. (e) Specific capacitance normalised by BET surface area at varying current densities. (f) Charge transfer resistance (R_{ct}) and ionic diffusion coefficients (D) calculated from electrochemical impedance spectroscopy.

The high desalination performance of G@MC-O-thin material represents a significant improvement over current materials used in commercial CDI systems.[3,6] The use of low cost electrochemically exfoliated graphene in G@MC synthesis facilitates the cost effective and saleable production of electrode materials. Moreover, the developed prototype CDI cell (Figure S2) can serve as single module in large CDI systems. With multiple, series-connected CDI cells, high performance desalination devices with compatible capability and lower operating cost to reverse osmosis systems could be fabricated.

Table 2. Electrochemical and electrosorption results for G@MC materials.

This journal is © The Royal Society of Chemistry 20xx

Please do not adjust margins

	SAC mg g^{-1}	SAC/S_{BET} x 10^{-2} mg m^{-2}	Cap. F g^{-1}	Cap./S_{BET} x 10^{-2} F m^{-2}	R_{ct} Ω	σ Ω $Hz^{1/2}$	D_{ionic} x 10^{-14} cm^2 s^{-1}
G@MC-O-thin	24.3	1.91	125.7	9.90	6.37	1.72	4.79
G@MC-PO-thin	22.2	2.02	77.0	7.00	7.54	2.11	3.18
G@MC-PO-thick	17.1	1.85	75.5	8.17	10.5	4.87	0.597
G@MC-C-thick	11.9	1.47	53.9	6.68	25.2	6.42	0.343

Conclusions

In summary, layered G@MC heterostructures with controllable mesopore openings and mesopore lengths were developed and applied as CDI electrode materials to evaluate the impact of pore accessibility on deionization performances. G@MC material with reduced mesopore layer thickness and open axially aligned pores showed enhanced CDI performance, when compared with similar structured materials with thicker layers or more obstructed mesopore openings. Based on material characterisations, CDI tests and electrochemical measurements, we conclude that the mesopore accessibility of CDI electrodes and the ion diffusion property within electrodes are largely determined by the mesopore opening and mesopore length. Rationally design the porous structure to improve the mesopore accessibility could greatly facilitate the ion influx from bulk solution into electrode pores and consequently promote the CDI performance. These findings and the novel materials shed new light on the development of high performance CDI electrodes.

Conflicts of interest

There are no conflicts to declare.

Acknowledgements

The authors acknowledge the financial support from the Australian Research Council, the Queensland Government, the CAS/SAFEA International Partnership Program for Creative Research Teams, the Australian National Fabrication Facility and the Australian Microscopy and Microanalysis Research Facility at the Centre for Microscopy and Microanalysis, The University of Queensland.

Notes and references

1. Suss, M. E.; Porada, S.; Sun, X.; Biesheuvel, P. M.; Yoon, J.; Presser, V., Water desalination via capacitive deionization: what is it and what can we expect from it? *Energy Environ. Sci.* **2015**, *8*, 2296-2319.
2. Al Marzooqi, F. A.; Al Ghaferi, A. A.; Saadat, I.; Hilal, N., Application of Capacitive Deionisation in water desalination: A review. *Desalination* **2014,** *342*, 3-15.
3. Oren, Y., Capacitive deionization (CDI) for desalination and water treatment — past, present and future (a review). *Desalination* **2008,** *228*, 10-29.
4. John W, B.; George W, M., Electrochemical Demineralization of Water with Porous Electrodes of Large Surface Area. In *SALINE WATER CONVERSION*, American Chemical Society: **1960**, *27*, 206-223.
5. Liu, Y.; Nie, C.; Liu, X.; Xu, X.; Sun, Z.; Pan, L., Review on carbon-based composite materials for capacitive deionization. *RSC Adv.* **2015,** *5*, 15205-15225.
6. Porada, S.; Zhao, R.; van der Wal, A.; Presser, V.; Biesheuvel, P. M., Review on the science and technology of water desalination by capacitive deionization. *Progress in Materials Science* **2013,** *58*, 1388-1442.
7. Peng, Z.; Zhang, D.; Shi, L.; Yan, T., High performance ordered mesoporous carbon/carbon nanotube composite electrodes for capacitive deionization. *J Mater Chem* **2012,** *22*, 6603-6612.
8. Tsouris, C.; Mayes, R.; Kiggans, J.; Sharma, K.; Yiacoumi, S.; DePaoli, D.; Dai, S., Mesoporous Carbon for Capacitive Deionization of Saline Water. *Environmental Science & Technology* **2011,** *45*, 10243-10249.
9. Zou, L.; Li, L.; Song, H.; Morris, G., Using mesoporous carbon electrodes for brackish water desalination. *Water Research* **2008,** *42*, 2340-2348.
10. Liu, P.; Yan, T.; Shi, L.; Park, H. S.; Chen, X.; Zhao, Z.; Zhang, D., Graphene-based materials for capacitive deionization. *Journal of Materials Chemistry A* **2017,** *5*, 13907-13943.
11. Shi, W.; Li, H.; Cao, X.; Leong, Z. Y.; Zhang, J.; Chen, T.; Zhang, H.; Yang, H. Y., Ultrahigh Performance of Novel Capacitive Deionization Electrodes based on A Three-Dimensional Graphene Architecture with Nanopores. *Scientific Reports* **2016,** *6*, doi:10.1038/srep18966.
12. Xu, X.; Pan, L.; Liu, Y.; Lu, T.; Sun, Z.; Chua, D. H. C., Facile synthesis of novel graphene sponge for high performance capacitive deionization. *Sci. Rep.* **2015,** *5*, doi: 10.1038/srep08458.
13. Xu, X.; Sun, Z.; Chua, D. H. C.; Pan, L., Novel nitrogen doped graphene sponge with ultrahigh capacitive deionization performance. *Scientific Reports* **2015,** *5*, doi: 10.1038/srep11225
14. Xu, X.; Tang, H.; Wang, M.; Liu, Y.; Li, Y.; Lu, T.; Pan, L., Carbon spheres with hierarchical micro/mesopores for water desalination by capacitive deionization. *Journal of Materials Chemistry A* **2016,** *4*, 16094-16100.
15. Li, Y.; Qi, J.; Li, J.; Shen, J.; Liu, Y.; Sun, X.; Shen, J.; Han, W.; Wang, L., Nitrogen-Doped Hollow Mesoporous Carbon Spheres for Efficient Water Desalination by Capacitive Deionization. *ACS Sustainable Chemistry & Engineering* **2017,** *5*, 6635-6644.
16. Wang, H.; Shi, L. Y.; Yan, T. T.; Zhang, J. P.; Zhong, Q. D.; Zhang, D. S., Design of graphene-coated hollow mesoporous carbon spheres as high performance electrodes for capacitive deionization. *Journal of Materials Chemistry A* **2014,** *2*, 4739-4750.
17. Li, Y.; Hussain, I.; Qi, J.; Liu, C.; Li, J.; Shen, J.; Sun, X.; Han, W.; Wang, L., N-doped hierarchical porous carbon derived from hypercrosslinked diblock copolymer for capacitive deionization. *Separation and Purification Technology* **2016,** *165*, 190-198.

Please do not adjust margins

18. Wen, X.; Zhang, D.; Yan, T.; Zhang, J.; Shi, L., Three-dimensional graphene-based hierarchically porous carbon composites prepared by a dual-template strategy for capacitive deionization. *J Mater Chem A* **2013,** *1*, 12334-12344.
19. Zornitta, R. L.; García-Mateos, F. J.; Lado, J. J.; Rodríguez-Mirasol, J.; Cordero, T.; Hammer, P.; Ruotolo, L. A. M., High-performance activated carbon from polyaniline for capacitive deionization. *Carbon* **2017,** *123*, 318-333.
20. Kim, C.; Srimuk, P.; Lee, J.; Fleischmann, S.; Aslan, M.; Presser, V., Influence of pore structure and cell voltage of activated carbon cloth as a versatile electrode material for capacitive deionization. *Carbon* **2017,** *122*, 329-335.
21. Li, G.-X.; Hou, P.-X.; Zhao, S.-Y.; Liu, C.; Cheng, H.-M., A flexible cotton-derived carbon sponge for high-performance capacitive deionization. *Carbon* **2016,** *101*, 1-8.
22. Wang, G.; Pan, C.; Wang, L.; Dong, Q.; Yu, C.; Zhao, Z., Activated carbon nanofiber webs made by electrospinning for capacitive deionization. *Electrochim Acta* **2012,** *69*, 65–70.
23. Noked, M.; Avraham, E.; Soffer, A.; Aurbach, D., The rate-determining step of electroadsorption processes into nanoporous carbon electrodes related to water desalination. *J Phys Chem C* **2009,** *113*, 21319-21327.
24. Li, L.; Zou, L.; Song, H.; Morris, G., Ordered mesoporous carbons synthesized by a modified sol–gel process for electrosorptive removal of sodium chloride. *Carbon* **2009,** *47*, 775-781.
25. Peng, Z.; Zhang, D.; Shi, L.; Yan, T.; Yuan, S.; Li, H., Comparative electroadsorption study of mesoporous carbon electrodes with various pore structures. *J Phys Chem C* **2011,** *115*, 17068-17076.
26. Zhang, D.; Wen, X.; Shi, L.; Yan, T.; Zhang, J., Enhanced capacitive deionization of graphene/mesoporous carbon composites. *Nanoscale* **2012,** *4*, 5440-5446.
27. Leong, Z. Y.; Lu, G.; Yang, H. Y., Three-dimensional graphene oxide and polyvinyl alcohol composites as structured activated carbons for capacitive desalination. *Desalination* **2017**, doi.org/10.1016/j.desal.2017.07.018.
28. Parvez, K.; Wu, Z.-S.; Li, R.; Liu, X.; Graf, R.; Feng, X.; Müllen, K., Exfoliation of Graphite into Graphene in Aqueous Solutions of Inorganic Salts. *Journal of the American Chemical Society* **2014,** *136* , 6083-6091.
29. Qu, K.; Zheng, Y.; Dai, S.; Qiao, S. Z., Polydopamine-graphene oxide derived mesoporous carbon nanosheets for enhanced oxygen reduction. *Nanoscale* **2015**, *7*, 12598-12605.
30. Noonan, O.; Zhang, H.; Song, H.; Xu, C.; Huang, X.; Yu, C., In situ Stober templating: facile synthesis of hollow mesoporous carbon spheres from silica-polymer composites for ultra-high level in-cavity adsorption. *Journal of Materials Chemistry A* **2016**, *4*, 9063-9071.
31. Carcouët, C. C. M. C.; van de Put, M. W. P.; Mezari, B.; Magusin, P. C. M. M.; Laven, J.; Bomans, P. H. H.; Friedrich, H.; Esteves, A. C. C.; Sommerdijk, N. A. J. M.; van Benthem, R. A. T. M.; de With, G., Nucleation and Growth of Monodisperse Silica Nanoparticles. *Nano Lett.* **2014,** *14*, 1433-1438.
32. Morishige, K.; Nakamura, Y., Nature of Adsorption and Desorption Branches in Cylindrical Pores. *Langmuir* **2004,** *20*, 4503-4506.
33. Del Frari, D.; Bour, J.; Ball, V.; Toniazzo, V.; Ruch, D., Degradation of polydopamine coatings by sodium hypochlorite: A process depending on the substrate and the film synthesis method. *Polymer Degradation and Stability* **2012,** *97*), 1844-1849.
34. Masalov, V. M.; Sukhinina, N. S.; Kudrenko, E. A.; Emelchenko, G. A., Mechanism of formation and nanostructure of Stober silica particles. *Nanotechnology* **2011,** *22*), 275718.
35. Stöber, W.; Fink, A.; Bohn, E., *J. Colloid Interface Sci.* **1968,** *26*, 62.
36. Hu, C. C.; Chu, C. H., Electrochemical impedance characterization of polyaniline-coated graphite electrodes for electrochemical capacitors: effects of film coverage/thickness and anions. *J Electroanal Chem* **2001,** *503*, 105-116.
37. Izadi-Najafabadi, A.; Futaba, D. N.; Iijima, S.; Hata, K., Ion Diffusion and Electrochemical Capacitance in Aligned and Packed Single-Walled Carbon Nanotubes. *Journal of the American Chemical Society* **2010,** *132*, 18017-18019.
38. Liu, Y.; Zhang, H.; Song, H.; Noonan, O.; Liang, C.; Huang, X.; Yu, C., Single-Layered Mesoporous Carbon Sandwiched Graphene Nanosheets for High Performance Ionic Liquid Supercapacitors. *The Journal of Physical Chemistry C* **2017,** *121*, 23947-23954.
39. Feng, M.; Du, Q.; Su, L.; Zhang, G.; Wang, G.; Ma, Z.; Gao, W.; Qin, X.; Shao, G., Manganese oxide electrode with excellent electrochemical performance for sodium ion batteries by pre-intercalation of K and Na ions. *Scientific Reports* **2017,** *7*, 2219.

This journal is © The Royal Society of Chemistry 20xx
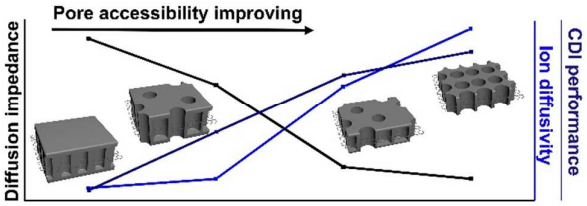
Layered graphene/mesoporous carbon heterostructures with controllable mesopore opening and pore length are synthesized, and demonstrate outstanding desalination performances.